Acta Materialia 160 (2018) 147–157

Contents lists available at ScienceDirect

Acta Materialia

journal homepage: www.elsevier.com/locate/actamat

Full length article

Structural and mechanical characterization of heterogeneities in a CuZr-based bulk metallic glass processed by high pressure torsion

Christian Ebner [a], Benjamin Escher [b], Christoph Gammer [c], Jürgen Eckert [c], Simon Pauly [b], Christian Rentenberger [a, *]

[a] Physics of Nanostructured Materials, Faculty of Physics, University of Vienna, Boltzmanngasse 5, 1090, Vienna, Austria
[b] Institute for Complex Materials, Leibniz Institute for Solid State and Materials Research Dresden, Helmholtzstraße 20, 01069, Dresden, Germany
[c] Erich Schmid Institute of Materials Science, Austrian Academy of Sciences, Jahnstrasse 12, 8700, Leoben, Austria

ARTICLE INFO

Article history:
Received 8 May 2018
Received in revised form
17 August 2018
Accepted 18 August 2018
Available online 31 August 2018

Keywords:
Bulk metallic glasses
High pressure torsion
Nanoindentation
Synchrotron X-ray diffraction
Rejuvenation

ABSTRACT

$Cu_{45}Zr_{45}Al_5Ag_5$ bulk metallic glass samples, processed by high pressure torsion (HPT) under various conditions, were characterized using synchrotron X-ray diffraction, nanoindentation, differential scanning calorimetry, atomic force and transmission electron microscopy. The experimental results clearly show that HPT modifies the amorphous structure by increasing the mean atomic volume. The level of rejuvenation, correlated with the excess mean atomic volume, is enhanced at higher shear strains as inferred from relaxation enthalpies. By mapping of structural and mechanical quantities, the strain-induced rejuvenated state is characterized on cross-sectional HPT samples on a local scale. A clear correlation both between elastic and plastic softening and between softening and excess mean atomic volume is obtained. But also the heterogeneity of the HPT induced rejuvenation is revealed, resulting in the formation of highly strain-softened regions next to less-deformed ones. A hardness drop of up to 20% is associated with an estimated increase of the mean atomic volume of up to 0.75%. Based on synchrotron X-ray diffraction and nanoindentation measurements it is concluded that elastic fluctuations are enhanced in the rejuvenated material on different length scales down to atomic scale. Furthermore, the calculated flexibility volume and the corresponding average mean square atomic displacement is increased. The plastic response during nanoindentation indicates that HPT processing promotes a more homogeneous-like deformation.

1. Introduction

Bulk metallic glasses (BMGs) are interesting materials because of their exceptional strength and high elastic limit [1,2]. These desired properties unfortunately come with the major drawback of almost non-existing tensile ductility. This is attributed to the lack of strain hardening mechanisms and the resulting localized deformation via shear bands (SBs) at temperatures below the glass transition temperature, T_g [3]. Scanning transmission electron microscopy studies indicate that SBs are thin bands (about 10–200 nm wide) carrying the plastic deformation and weakening the material locally [4–6]. Thereby they modify the structural motifs and introduce local density fluctuations with an overall increase in free volume (FV) [4,7]. Critical failure finally occurs by cavities along soft SBs [8]. FV has been attributed as an important parameter in understanding the mechanical properties of BMGs. Fully understanding the elastic and plastic deformation in BMGs, however, remains a scientific challenge which has to be overcome to render these materials suitable for structural applications [9–11].

Shear transformation zones (STZs) are believed to be the operational entities for SB nucleation. They are localized unstable volumes, which rearrange under critical external stresses [12]. If the stresses reach the yield stress, a large number of STZs in direction of maximal resolved shear stress are activated until finally the SB nucleates and carries the deformation. By frictional heat release not only the narrow SB is deformed, but also its surrounding is affected, promoting further strain softening [13,14]. Also, long-range stress fields are introduced by the SBs [8] and the failure by a single critical SB renders BMGs brittle.

Tailoring heterogeneities into the glassy structure has been

* Corresponding author.
E-mail address: christian.rentenberger@univie.ac.at (C. Rentenberger).

https://doi.org/10.1016/j.actamat.2018.08.032

suggested as a way to overcome limitations by brittleness [11]. Heterogeneities can affect SB propagation and can increase the number of possible nucleation sites for new SBs. By interaction and spread of SBs over a larger sample volume a more uniform deformation can be achieved. Recently, different sample pre-treatment methods have shown to give promising results. For example, imprinting has been shown to introduce stress heterogeneities [15]. Thermal cycling between liquid nitrogen and room temperature increases the structural heterogeneities and improves the BMGs properties [16]. By this treatment, the maximum compressive strains reached prior to failure can be increased. Also, severe plastic deformation (SPD) by high pressure torsion (HPT) significantly increases ductility [17–19]. HPT can introduce a high density of SBs without the material failing because of the geometric confinement and high hydrostatic pressures [20]. Additionally, introduction of residual stresses can be achieved by this method and might be beneficial for the plasticity [21], as well as structural disordering and creation of excess FV (rejuvenation) [22]. Therefore, the characterization of structural modifications occurring during HPT are of great interest. Nanoindentation has proven to be a suitable method for investigating the local mechanical properties of BMGs [23,24] and especially the properties near SBs in mechanically deformed specimens [5,8,13]. In addition, the method is sensitive to local stress fields and might be used to map stress gradients in BMGs [25,26].

In this study, we present the microstructural changes of a high glass-forming $Cu_{45}Zr_{45}Al_5Ag_5$ alloy [27] subjected to SPD by the method of HPT. A strong structural gradient along the axial direction is formed in the material during room temperature (RT) HPT deformation up to a nominal shear strain of about 500 000% under a quasi-hydrostatic pressure of 4 GPa or 8 GPa. This has not been reported in literature so far and is of great importance for follow-up measurements. By 2-D mapping of cross-sections via synchrotron X-ray diffraction and nanoindentation we systematically quantify these structural heterogeneities and show their effect on the local mechanical properties. In addition, analysis of structural relaxation upon heating by differential scanning calorimetry (DSC) is performed. We investigate and discuss the change in mean atomic volume and plastic response of the HPT processed specimens. Results are compared to the undeformed as-cast state.

2. Methods

$Cu_{45}Zr_{45}Al_5Ag_5$ BMG master alloy ingots ((25 ± 1)g) were prepared by arc melting of high purity elements (Al, Cu: 99.99 wt%, Ag: 99.9 wt%, Zr: 99.8 wt%) under a Titanium gettered Ar atmosphere. Inductively-coupled plasma optical emission spectroscopy (ICP-OES, Thermo Scientific IRIS Intrepid II XUV and iCAP 6000) was used to control the composition. The ingots were cast with a suction casting device (Bühler AM) using a water cooled Copper mould into plates with dimensions of 1.5 mm × 10 mm × 80 mm. The amorphous state of the as-cast specimen was confirmed by transmission electron microscopy (TEM) as well as by X-ray diffraction using a PANalytical X'Pert Pro (reflection, 30°-70° Co K-alpha).

HPT processing of disc shaped samples with 8 mm diameter was performed. The discs were punched from $Cu_{45}Zr_{45}Al_5Ag_5$ BMG plates by electric discharge processing and mechanically ground to 550 μm thickness prior to deformation. The surface of the samples as well as the anvils of the HPT device were roughened by sandblasting to increase friction and avoid slipping. Several specimens were subjected to 80 turns of HPT processing with a quasi-hydrostatic pressure of 4 GPa or 8 GPa at RT. Additional discs were processed by HPT at liquid nitrogen temperature (LNT) up to 20 turns using a pressure of 8 GPa. Processing was carried out with a speed of 0.2 rpm to avoid heating. Finally, deformation by compression only (8 GPa for 25 min) was used to check the influence of the initial compression on the microstructure.

For nanoindentation, cross-sections of the HPT processed specimens were prepared by cutting a central stripe of ≈ 1 mm width by electric discharge processing. These stripes were embedded into a support and carefully ground from both sides to remove layers affected by cutting. A root mean square roughness of 6 nm was obtained by polishing with 300 nm average grain size alumina polishing paste, as measured by atomic force microscopy (AFM). Nanoindentation was conducted on the cross-sections using the ASMEC Unat nanoindenter. A Berkovich indenter geometry and a maximum load of $P_{max} = 50$ mN was used for the measurements. A large portion of the cross-sectional area was mapped by more than 1000 indentations for each of the samples with 100 μm spacing in the radial direction and 10 μm over the height. Resulting load-displacement curves were analysed by the standard Oliver-Pharr method [28] to extract hardness and Young's modulus values with a Poisson's ratio of $\nu = 0.3722$ [29]. Each curve included a 30 s hold segment at P_{max} and a 60 s hold segment at 10% of P_{max} for thermal drift correction. All load-displacement curves were zero-point corrected by fitting a Hertzian model function and corrected for thermal drift using the InspectorX software from ASMEC. Reference measurements were performed on as-cast specimens.

Material pile-up behaviour surrounding nanoindents was checked by AFM measurements using a WITec alpha 300 A. The measurements were performed in AC mode using standard tips with 512 pixel × 512 pixel covering an area of 15 μm × 15 μm at a scan speed of 3 s/line. The data was analysed using the Gwyddion software [30]. Only a few selected imprints were measured for each of the deformation states because of the slow scan speed needed to obtain a good quality topographic dataset.

Synchrotron diffraction mapping was carried out at the beamline ID31 at the ESRF in Grenoble. The cross-sections of the HPT processed discs were mechanically thinned to 500 μm thickness prior to the experiment. Diffraction patterns were recorded with a beam energy of 78 keV, a beam shape of 30 μm × 15 μm and a Pilatus3xCdTe-2M detector. The maps were acquired with 200 μm spacing in radial direction and 20 μm spacing over the height, covering nearly the full cross-sectional area. Line profiles were obtained by azimuthal integration of the 2-D diffraction patterns. The peak maxima position of the 1st peak $q_1 = \frac{4\pi}{\lambda}\sin(\theta/2)$ as well as their half width at half maximum (HWHM), a, and intensity, I, were extracted from the line profiles by fitting the following pseudo-Voigt model function $pV(q)$ to the line profiles.

$$G(q) = I_g \cdot \exp\left(-\ln(2)\cdot[(q-q_1)/a]^2\right) \quad (1)$$

$$L(q) = \frac{I_l}{1+[(q-q_1)/a]^2} \quad (2)$$

$$pV(q) = \eta \cdot G(q) + (1-\eta)\cdot L(q) + k\cdot q + d \quad (3)$$

Here I_g and I_l denote the intensities of the Gaussian and Lorentzian curve, η is the mixing parameter and k and d are the slope and offset of a linear background. Up to 400 diffraction patterns were acquired for each specimen in a unique and unprecedented cross-sectional mapping.

Relaxation enthalpies were obtained from DSC measurements using a power compensated PerkinElmer DSC 6200. Heat flow was measured during isochronal heating with a heating rate of 20 K min^{-1}. The samples were prepared from same radial positions near the edge of the HPT discs and heated in 3 steps: a first run from RT up to T_g to anneal free volume accumulated by the deformation, a second run from RT up to 823 K, which is above the crystallisation

temperature of the BMG, and finally a third run from RT to 823 K. After each heating step, isothermal equilibration at the corresponding temperature is performed for 10 min, followed by isochronal cooling to RT (100 K min^{-1}). By using the third run as baseline for the second, the crystallisation temperatures were obtained. The heat flow from the second run was subtracted from the first one to extract the relaxation enthalpy attributed to the FV annealing.

TEM specimens of all different deformation states were thinned by electropolishing in a Struers Tenupol 3 using an electrolyte of 33% nitric acid and 66% methanol at 4 V potential and ≈ 250 K. Bright-field and dark-field images as well as diffraction patterns were taken with a Philips CM200 TEM operating at 200 kV in order to check for structural changes such as crystallisation.

3. Results

3.1. High pressure torsion processing of CuZr based metallic glasses

The $Cu_{45}Zr_{45}Al_5Ag_5$ BMG with limited compression ductility [31] was successfully deformed under various HPT conditions to very high nominal shear strains of up to 500 000%. The initial specimen thickness of 550 μm is reduced to about 300 μm–400 μm post-deformation for all the specimen by material flow at the gap between the anvils. The flow is especially pronounced in the early stage (compression and low number of rotations). No cracking of the specimens is observed even after SPD up to 80 turns and no slipping occurred as checked by surface markers. X-ray diffraction and TEM studies (cf. Fig. A1) of the deformed specimens rule crystallisation out, since they show only characteristic features of a fully amorphous structure.

A small explosion (observed for small shear deformations corresponding to a rotation angle of 15°–30 °) is reproducible in case of deformations using 8 GPa. The explosion is not present for deformations at 4 GPa and under liquid nitrogen and might be explained by rapid oxidation of material squeezed out during the propagation of the first SBs. A similar phenomenon has been observed during fracture tests using V-notched impact specimens [32]. The successful deformation of the specimens even at LNT demonstrates the high deformability of the present CuZr-based BMG alloy under geometrical constraints.

3.2. Mapping of microstructural inhomogeneities by nanoindentation

Nanoindentation studies performed on the cross-sections of discs after HPT processing reveal a strong heterogeneity in the mechanical properties. Fig. 1 shows the 2-D cross-section maps of the hardness for the HPT discs deformed by 20 turns/8 GPa/LNT, 80 turns/8 GPa/RT and 80 turns/4 GPa/RT. All maps were normalized by the average as-cast hardness.

The specimen deformed by 20 turns/8 GPa/LNT shows a radial decrease in hardness, which is in agreement with the increasing nominal shear strain $\gamma = 2\pi rN/h$, r being the radial distance from the rotation centre, N the number of turns and h the sample thickness. There is a decrease of the hardness of up to 15% for the highly strained regions.

For both specimens processed up to 80 turns at RT (cf. Fig. 1), a strong and sharp gradient of the hardness over the height is observed. A highly deformed plastic zone is formed with a reduced hardness of up to 20% as compared to the as-cast state. The volume fraction of this plastic zone gradually increases with increasing nominal accumulated shear strain in radial direction. The comparison between the two samples deformed at RT shows that a tendency to slightly higher fractions for the 4 GPa specimen exists. This is confirmed by the relaxation enthalpies as will be discussed later. The less deformed regions, neighbouring the highly deformed ones, show a local variation in hardness comparable to the central part ($r < 1000$ μm) of the specimen deformed 20 turns at LNT. The Young's modulus maps (cf. Fig. 2) reveal a strong correlation

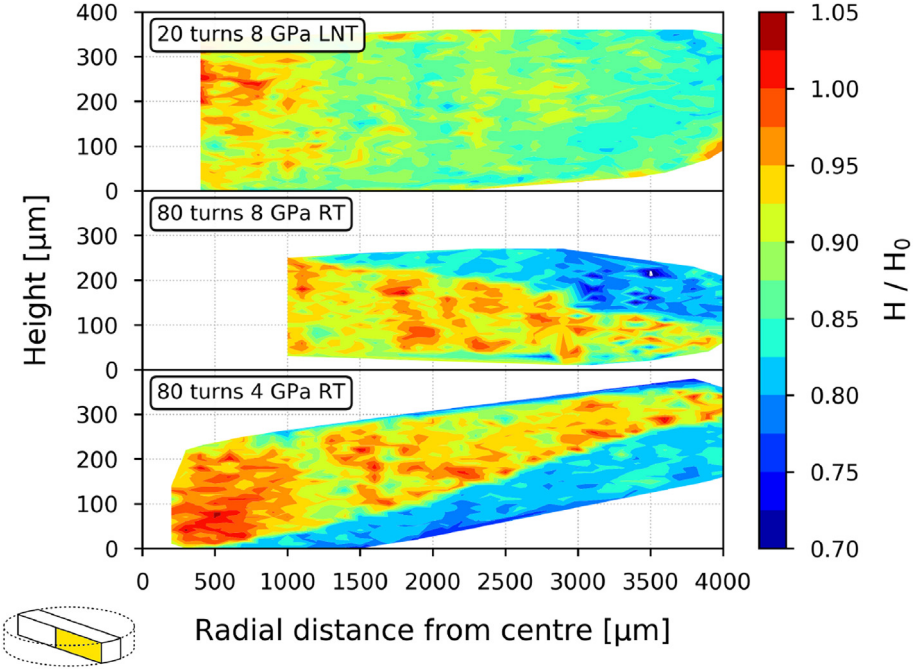

Fig. 1. Hardness maps of HPT disc cross-sections: Hardness values (H) measured for the HPT discs were normalized by the as-cast hardness (H_0). The mapping reveals a strongly inhomogeneous microstructure and the evolution of large, highly strain-softened zones. Cross-sections of the HPT deformed specimens were prepared from the central region of the discs as illustrated in the inset. Nanoindentation and synchrotron X-ray diffraction measurements were conducted on the surface indicated in yellow. (For interpretation of the references to colour in this figure legend, the reader is referred to the Web version of this article.)

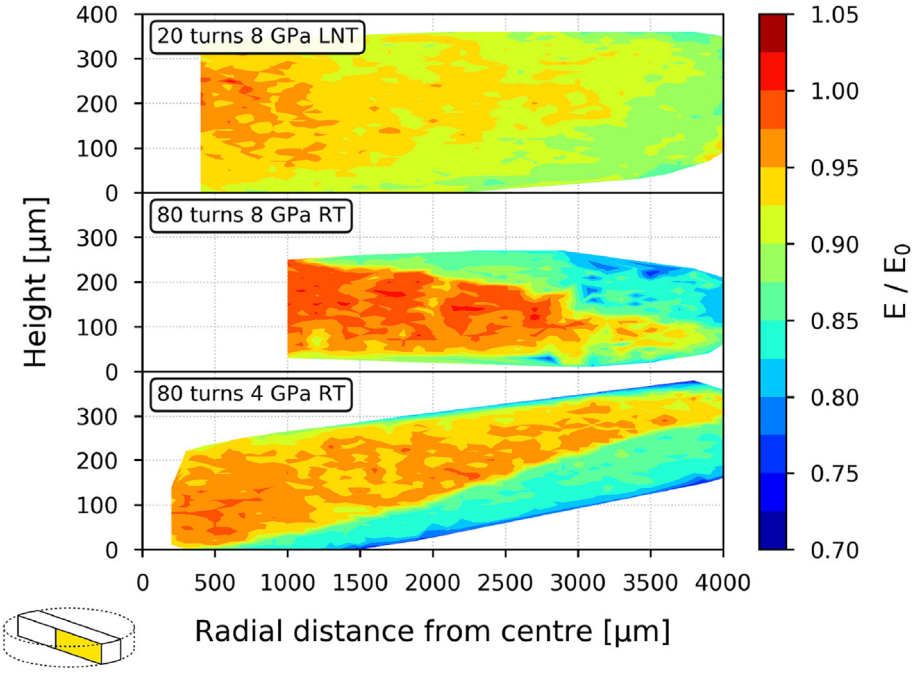

Fig. 2. Young' s modulus maps of HPT disc cross-sections: Young's modulus values (E) were normalized by the Young's modulus of the as-cast state (E_0). A clear decrease of the Young's modulus for positions of reduced hardness is observed. This change in elastic properties indicates a structural change at atomic level.

between the hardness and the elastic properties and therefore follow the same trend in heterogeneity. The drop in Young's modulus in the plastic zones of both specimens deformed by 80 turns is up to 20%.

Statistical quantification of the absolute hardness and Young's modulus data was carried out by calculating mean and standard deviation. Fig. A2 shows the hardness frequency plot for different deformation states. Indentation of the as-cast reference $Cu_{45}Zr_{45}Al_5Ag_5$ specimens shows a sharp unimodal distribution of hardness with an average value of (5.95 ± 0.16) GPa indicating a homogeneous microstructure. For the specimen deformed by 20 turns/8 GPa/LNT the distribution becomes broader and is shifted to lower values with an average of (5.30 ± 0.23) GPa. This shift is based on the observed radial strain softening occurring during deformation. In case of the specimens deformed by 80 turns at 4 or 8 GPa, a bimodal hardness distribution is obtained. For the sample deformed at 4 GPa the average hardness in the soft regions is (4.87 ± 0.10) GPa, while the hard regions give (5.62 ± 0.21) GPa. For the sample deformed at 8 GPa an average hardness value of (4.87 ± 0.18) GPa is measured in the soft region, whereas (5.58 ± 0.18) GPa is obtained for the harder regions.

The same trends are observed in the elastic properties. Fig. A3 illustrates the frequency distribution of the Young's modulus. Here, the sharp unimodal distribution for the as-cast state gives an average Young's modulus of (103 ± 1) GPa. The values of the specimen deformed at 8 GPa by 20 turns are shifted to an average of (93.9 ± 2.5) GPa. The specimen deformed at 4 GPa shows (86.3 ± 2.5) GPa for the soft and (96.7 ± 2.0) GPa for the hard regions. For the specimen deformed at 8 GPa by 80 turns, the average Young's modulus is measured to be (87.1 ± 3.3) GPa in the soft regions and (98.0 ± 3.3) GPa in the hard regions. In order to probe different elastic volumes also the depth dependence of the Young's modulus was checked by ≈100 nanoindentation imprints over an area of about 150 µm × 350 µm in the soft regions. The results show that the Young's modulus is independent of the contact depth for values larger than 100 nm. Despite of that, the scatter of the measured values is increased in the strain softened regions as compared to the as-cast state, indicating an increased heterogeneity of the elastic properties.

Pile-up effects during instrumented indentation can have a significant influence on the experimentally measured absolute values and have to be taken into consideration [26]. AFM topographies of selected indents show a significant pile-up area in the order of about 15%–25% for all the measured indents (cf. Fig. A4). However, the structural modification by HPT did not significantly reduce the pile-up formation in our measurement. Therefore, due to the limited number of measurements and the large scatter of the measured inner pile-up areas, no correction of the obtained hardness and Young's modulus values is performed and all values are instead plotted relative to the as-cast state. Nevertheless, the plastic zone surrounding the indents in HPT processed samples exhibits a significant reduction in the number of shear steps. Exemplary line profiles of the indents can be seen in Fig. A4(c). This indicates a change of the plastic behaviour by HPT processing.

3.3. Structural changes measured by synchrotron X-ray diffraction

The synchrotron peak positions of the first intense diffraction halo q_1 was analysed after extraction from the diffraction patterns. Fig. 3 shows the spatially resolved shift of the first diffraction peak q_1 by plotting the ratio $q_1/q_{1,0}$; the latter value $q_{1,0}$ is calculated by averaging over a cross-sectional area near the disc centre ($r < 400$ µm). A systematic shift to smaller values of q_1 is observed for the highly strained regions of the specimens. This is especially pronounced in the specimen deformed up to 80 rotations. By comparison with the nanoindentation maps in Figs. 1 and 2, the correlation of the peak shifts with the change in mechanical properties becomes evident. Since the shifts can be correlated with a change in the mean atomic volume $\overline{\Omega}$ [33], the observed shifts are consistent with an increase of the excess FV in strain-softened regions.

Fig. 4 shows the full width at half maximum (FWHM) for q_1

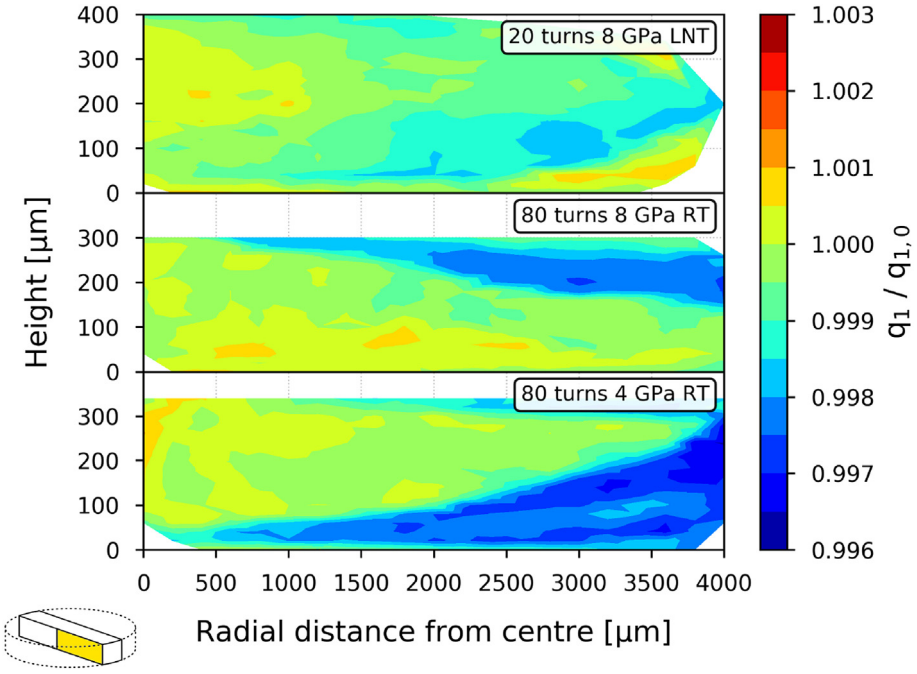

Fig. 3. Relative peak shift of q_1 obtained from synchrotron X-ray diffraction: The peak position of the first diffraction peak q_1 normalized to the mean value $q_{1,0}$ (averaged over $r < 400$ µm) is mapped over the cross-sections of the HPT deformed discs. The variation of the ratio correlates with the mechanical properties. In the highly deformed regions q_1 shifts to smaller values, indicating an increase in the mean atomic volume and therefore the creation of a rejuvenated structure with excess FV.

normalized to that of $q_{1,0}$. The measurement reveals an increase of the FWHM for the strain softened regions. In addition, the FWHM maps exhibit a direct correlation with the maps illustrating the peak shifts (cf. Fig. 3). The time between some of the HPT deformations and their synchrotron measurements was more than a year. Therefore it is safe to state that the strain-induced structural change in the SPD zones are stable over a long time at RT.

3.4. Free volume annealing by DSC

DSC measurements of all the deformation states demonstrate a trend matching the previous results. Fig. 5 shows the difference in specific heat capacity, Δc_p, caused by structural relaxation during the first run of the different states. The as-cast curve shows only a small signal of $\Delta H = 0.38 \pm 0.07$ kJmol^{-1} near T_g, indicating that the

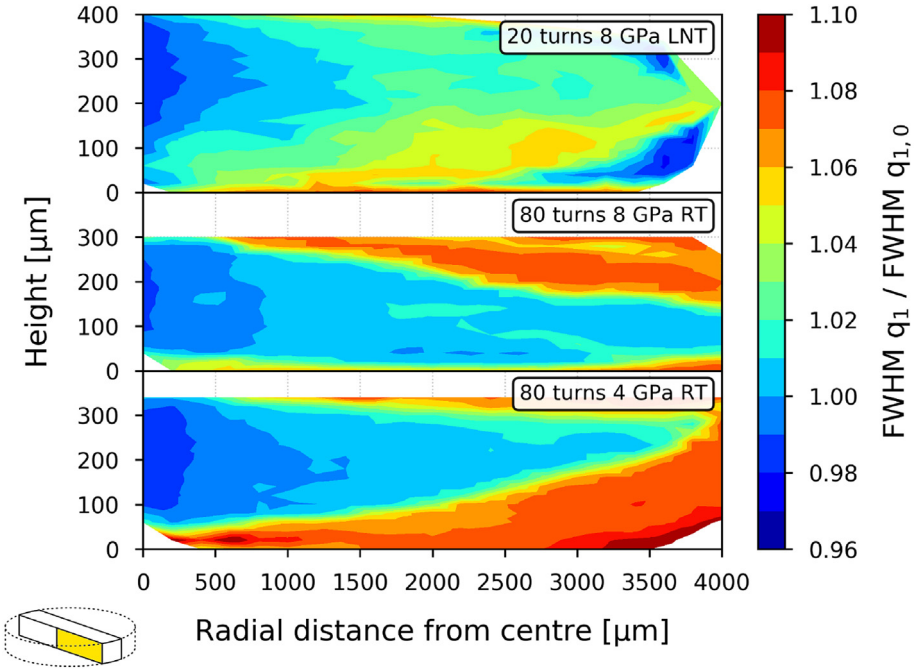

Fig. 4. Relative FWHM change of peak q_1: The change in FWHM for the first diffraction peak q_1 with respect to the mean value $q_{1,0}$ (averaged over $r < 400$ µm) is mapped over cross-sections of the HPT deformed discs and indicates an increase in structural heterogeneity by rejuvenation using HPT deformation. In the highly deformed regions the FWHM of q_1 increases considerably.

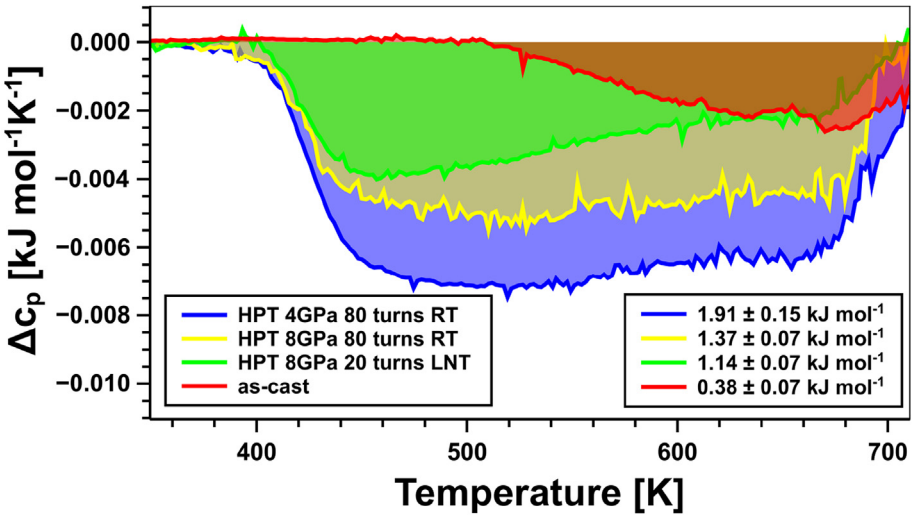

Fig. 5. Relaxation enthalpies from DSC: The relaxation heat capacity of the as-cast and HPT deformed BMG samples. The relaxation enthalpy (ΔH) gradually increases with increased severely deformed volume content. The onset of relaxation is around 410 K for all plastically deformed specimen.

specimens after suction mould casting are close to a relaxed state. The onset of relaxation is at ≈510 K for this case. The relaxation enthalpies for the HPT deformed specimens show a clear trend: with increasing volume fraction of strain-softened regions, the relaxation enthalpies increase. In the case of HPT deformation by 20 turns/8 GPa/LNT, the signal increases to $\Delta H = (1.14 \pm 0.07)$ kJmol^{-1} and the relaxation onset is decreased by about 100 K to ≈410 K. The relaxation signals increase further by increased shear deformation, leading to $\Delta H = (1.37 \pm 0.07)$ kJmol^{-1} for the HPT 80 turns/8 GPa/RT specimen and even $\Delta H = (1.91 \pm 0.15)$ kJmol^{-1} for the HPT 80 turns/4 GPa/RT specimen. For both cases the relaxation onset is again about 410 K. Since the measured signals are integral values a composite model was used (cf. section 4.2) to estimate the relaxation enthalpy of the severely deformed volume of the 80 turns/4 GPa/RT specimen (bluish area in Fig. 1). By taking the geometry and axial heterogeneity of the DSC sample into account, the estimation gives a value of $\Delta H \approx 3.44$ kJmol^{-1}. It is safe to assume that the structural state of the HPT processed samples relaxes completely during the first run and any free volume is annealed, since in the second run there are no relaxation signals left (cf. Fig. A6). The measured relaxation enthalpies are large as compared to other methods of rejuvenation, such as elasto-static loading ($\Delta H = 0.42$ kJmol^{-1}) [34], cryogenic cycling ($\Delta H = 1.1$ kJmol^{-1}) [16] and elasto-dynamic loading ($\Delta H = 0.92$ kJmol^{-1}) [35]. Extraordinary values were reported for cryogenic DMA ($\Delta H = 5.1$ kJmol^{-1}) [36].

4. Discussion

4.1. Strain softening and formation of highly deformed plastic zones

For crystalline materials it is well known that SPD (e.g. using HPT) leads to deformation induced structural refinement that is correlated with the competition between generation and annihilation of lattice defects like vacancies, dislocations and grain boundaries. This competition limits the minimum grain size and leads to a steady-state regime where the defect generation and annihilation rates are in equilibrium [37]. In the case of materials showing strain hardening a homogeneous nanostructure is achieved over the HPT disc when a minimal strain threshold is exceeded. Contrary, if strain softening takes place, localized deformation is the direct consequence [38].

In the case of BMGs, it is expected that SPD leads to a structural modification of the amorphous phase that is limited by the competition between the generation and annihilation of 'defects' in the form of FV. The generation of FV is accomplished by plastic deformation via SBs whereas its annihilation is facilitated by recovery processes causing relaxation (see section 4.2). The resulting modified structure induced by SPD affects both elastic and plastic properties of BMGs considerably. Figs. 1 and 2 show that SPD of BMGs leads to a decrease of the hardness and the Young's modulus up to 20%, respectively. These changes of mechanical quantities are correlated with rejuvenation of the amorphous structure on atomic scale as revealed from the comparison with synchrotron X-ray diffraction experiments (cf. Fig. 3 and section 4.2). Rejuvenation attributed to FV is facilitated by the propagation of a high number of SBs, necessary to assure strain compatibility throughout the specimen. Introduction of FV during HPT is an intrinsic process of SB operation. Local structural changes within SBs create local FV and induce a surrounding stress field, causing some densification of this surrounding because of the spatial confinement. Upon unloading of the hydrostatic pressure, this boundary conditions are changed and the specimen volume increases by reducing these stress fields, leaving only some residual stresses. With increasing shear strain, more volume is affected by the deformation via SBs, generating further FV and expanding its fraction [13]. In the case of SPD by HPT, the superimposed back-pressure and the geometric confinement do not allow for cavitation and premature failure along SBs. This generally allows to reach much higher levels of rejuvenation compared to unconstrained plastic deformation of BMGs. Once the formation and relaxation rates of FV are equal, at least locally a saturated state of the modified amorphous structure can be reached. Due to the lower hardness of the rejuvenated structure, deformation will be continued primarily in this strain-softened area. As a consequence of strain softening, a strong heterogeneity of the modified structure on micron scale follows, leading to an inhomogeneous distribution of the local mechanical quantities. The evolution of these heterogeneous mechanical properties can be manifested already at the stage of pure compression. The heterogeneity is not necessarily correlated with the nominal shear strain of the HPT deformation since a strong structural gradient along the height evolves (cf. Fig. 1). This result shows that material flow can be concentrated near the upper or lower part of the HPT specimen leaving the other one less deformed. Therefore, even for HPT specimens with cylindrical

symmetry, 2-D mapping of the cross-section is essential to fully characterize their structural and mechanical properties. These results are also of importance for the interpretation of structural and mechanical measurements present in the literature [18,21,39,40], as well as for application.

Further understanding of the formation of the strong structural gradient along the axial direction during HPT processing can be obtained from finite element method (FEM) simulations [41]. These simulations demonstrate that the contact friction coefficient of the lateral anvil-specimen wall is a crucial parameter for the evolution of flow localization for strain softening materials. The specimen flows less and moves more like a rigid body on the side where it is constrained by a higher friction to the anvil wall, while flow is more concentrated to the side with lower friction. The difference in friction can be caused by slight variations in surface roughness as well as by initial strain localization near the surface as observed in Ref. [22]. Both of them are affected by pre-treatment using sandblasting. It should be mentioned that the formation of the structural gradient over the height is present already after HPT processing by 20 turns 8 GPa at RT (not shown) and becomes more evident for higher shear strains. However, by HPT processing by 20 turns 8 GPa at LNT (cf. Fig. 1) the heterogeneity along the axial direction is not as pronounced.

4.2. Excess mean atomic volume, free volume and flexibility volume

Rejuvenation of the amorphous structure by HPT deformation is attributed to the creation of excess mean atomic volume $\Delta\overline{\Omega} = \overline{\Omega} - \overline{\Omega}_0$ as revealed by synchrotron X-ray diffraction, showing a reduction of the scattering angle for the first diffraction peak q_1 (cf. Fig. 3). Additionally, the increase in FWHM of q_1 demonstrates a larger variety and therefore an increased heterogeneity of the atomic level structural features (see Fig. 4), indicating changes in short to medium range order for the deformed regions. This broadening is systematically correlated to the peak shift and shows that both are a consequence of plastic deformation.

In order to calculate the deformation-induced increase $\Delta\overline{\Omega}$ from the peak shift, q_1, the following approximation and measurements are used: Literature data of X-ray diffraction experiments of metallic glasses indicate a fractal (non-integer dimensional) scaling behaviour of the peak positions, q_1, and $\overline{\Omega}$ [33], although still under discussion [42]. The relation is found to be $q_1\overline{\Omega}^{0.433\pm0.007} = 9.3\pm0.2$, giving a fractal dimension of $D_f = 2.31$ [33]. Here, q_1 is given in $1/\text{Å}$ and $\overline{\Omega}$ in Å^3.

Based on the measured changes of q_1, we calculated the distribution of $\overline{\Omega}$ as shown in the histograms in Fig. A5. These distributions become broader and show a tendency to an increase of $\overline{\Omega}$ with increasing deformation. To compare the results with the as-cast sample and estimate $\Delta\overline{\Omega}$, a linear relationship between mean atomic volume and Young's modulus is used. In a first step, the histograms in Fig. A3 are fitted with Gaussian distributions as illustrated in Fig. 6 (a). The Gaussian maxima positions are then plotted against the maxima of the Gaussian fits for the histograms of $\overline{\Omega}$ (cf. Fig. A5), which are obtained in the same manner as illustrated in Fig. 6(b). By a linear fit the correlation between $\overline{\Omega}$ and the Young's modulus E is obtained over the whole range of experimental values (cf. Fig. 6(c)). The known average E value for the as-cast specimen (red point in Fig. 6(c)) finally gives an estimate of $\overline{\Omega}$ for the as-cast state ($\overline{\Omega}_0 \approx 17.14\text{Å}^3$). Comparing this value e.g. to the saturation value of $\overline{\Omega} = 17.27\text{Å}^3$ for the highly deformed regions of the specimen deformed by 80 turns, an estimated $\Delta\overline{\Omega}/\overline{\Omega}_0$ of 0.75% is obtained. This is significantly smaller than density changes inside shear bands measured by TEM [4,6,7], because synchrotron X-ray diffraction averages over a larger volume. The dashed line indicated in Fig. 6(c) represents the relationship between $\overline{\Omega}$ and E as reported in literature [43], obtained by a fit to multiple glass systems. This line strongly deviates from the experimental values of the present study and might therefore be used with care for systems rejuvenated by SPD methods. Also, it should be noted that in literature a relation $q_1 \propto \overline{\Omega}^{1/3}$ is reported [42]. However, this would lead to an even higher calculated value of $\Delta\overline{\Omega}$. In addition, the flexibility volume, v_{flex}, that is suggested by Ding et al. [44] as universal structural parameter correlating with relaxation and shear transformations, was calculated based on the local Young's modulus using $v_{\text{flex}} = 2(1+\nu)Ck_BT/E$ (with constant C given in Ref. [44]). The distribution of v_{flex} is presented in Fig. 6(d) for the 80 turns/4 GPa/RT specimen. The bimodal distribution gives $(0.055 \pm 0.002)\ \text{Å}^3$ for the less deformed and $(0.062 \pm 0.002)\ \text{Å}^3$ for the severely strained regions. Our values are in good agreement with the ones obtained from simulation [44].

According to the obtained relationship between mean atomic volume and Young's modulus (thick line in Fig. 6(c)), the local $\Delta\overline{\Omega}$ of the rejuvenated structure can be evaluated on micron scale on the basis of nanoindentation measurements as shown in Fig. 7(a). Furthermore, due to this relationship and the observed increase of the FWHM of q_1 (representing an increased variability of $\overline{\Omega}$ in strain softened regions), it can be concluded that elastic fluctuations are enhanced in the rejuvenated material on different length scales down to atomic scale. Since $<r^2> = v_{\text{flex}}/\sqrt[3]{\overline{\Omega}}$ [44], also the average mean square atomic displacement $<r^2>$ is accessible on micron scale by our experimental data. Fig. 7(b) shows the increase of $<r^2>$ for the rejuvenated regions, also confirming an increased atomic flexibility in this regions and indicating a reduced activation energy for structural relaxation [44]. This is consistent with the strain induced decrease of the temperature for the onset of relaxation measured by DSC (cf. Fig. 5).

Using the full exothermic relaxation signal below T_g experimental estimates for the increased FV can be extracted. The pronounced relaxation signal below T_g for HPT deformed specimens (see Fig. 5) is attributed to structural relaxation and annealing of FV [13,45,46]. The systematic increase in the relaxation enthalpy reflects the increased content in FV and implies again structural rejuvenation by HPT. Here, we calculate an estimate of the increased FV content for the highly deformed and rejuvenated regions for the specimen with the highest relaxation enthalpy (deformed by HPT 80 turns under pressure of 4 GPa at RT). The specimen geometry and heterogeneity of the deformation in axial direction (cf. Figs. 1–4) are taken into account by a simple two phase model. We assume the integral signal, ΔH_{avg}, to be composed of the volume fraction $v_i = V_i/V$ weighted sum of an as-cast enthalpy, $\Delta H_{\text{as-cast}}$, and an unknown enthalpy for the severely deformed regions, $\Delta H_{\text{deformed}}$, $\Delta H_{avg} = v_{\text{as-cast}}\Delta H_{\text{as-cast}} + v_{\text{deformed}}\Delta H_{\text{deformed}}$. The volume fractions for the relaxed specimen were estimated by taking the cross-sectional hardness measurements and the specimen geometry into account. This led to a volume fraction of $v_{\text{as-cast}} = 48.8\,\%$ and $v_{\text{deformed}} = 51.2\,\%$ for the sample used for relaxation, resulting in a value of $\Delta H_{\text{deformed}} = 3.44\text{kJmol}^{-1}$ (as already noted in section 3.4). By this, we finally obtain a FV of $\omega_{\text{deformed}} = 0.54\,\%$, using the relation $\Delta H_{\text{deformed}} = \beta\omega_{\text{deformed}}$, with $\beta = 642.1\text{kJmol}^{-1}$ [46]. This rough estimation of the FV increase is consistent with the estimated $\Delta\overline{\Omega}$ of 0.75% obtained from the X-ray diffraction.

4.3. Change in plastic response caused by structural rejuvenation

Structural rejuvenation of BMGs is accompanied by distinct changes in the plastic response. It is known that nanoindentation of BMGs at small loading rates typically shows discontinuities in the loading curve, attributed to SB activation [47–49]. The number and offsets of pop-ins giving information on the plastic behaviour of the

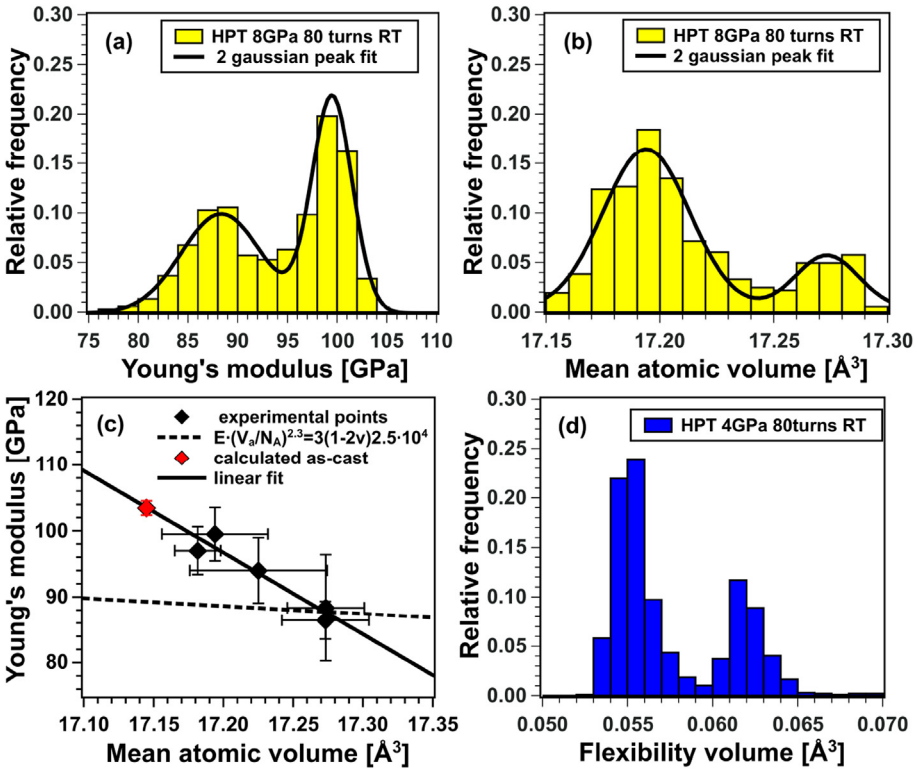

Fig. 6. Correlation of average atomic volume and Young's modulus: (a) The Young's modulus distribution as well as the average atomic volume (b) are fitted by Gaussian peaks for all the specimen as shown in this example. (c) The maxima positions of the Gaussian peak fits of the Young's modulus (a) are plotted against those of the mean atomic volume (b). Error bars are obtained from the peak widths of the fit. In addition the calculated data-point for the as-cast state is shown in red. The dashed line indicates the curve obtained by Ref. [43], the black line is a linear fit to the data points. (d) Exemplary flexibility volume distribution of a severely strained specimen calculated based on the experimental data. (For interpretation of the references to colour in this figure legend, the reader is referred to the Web version of this article.)

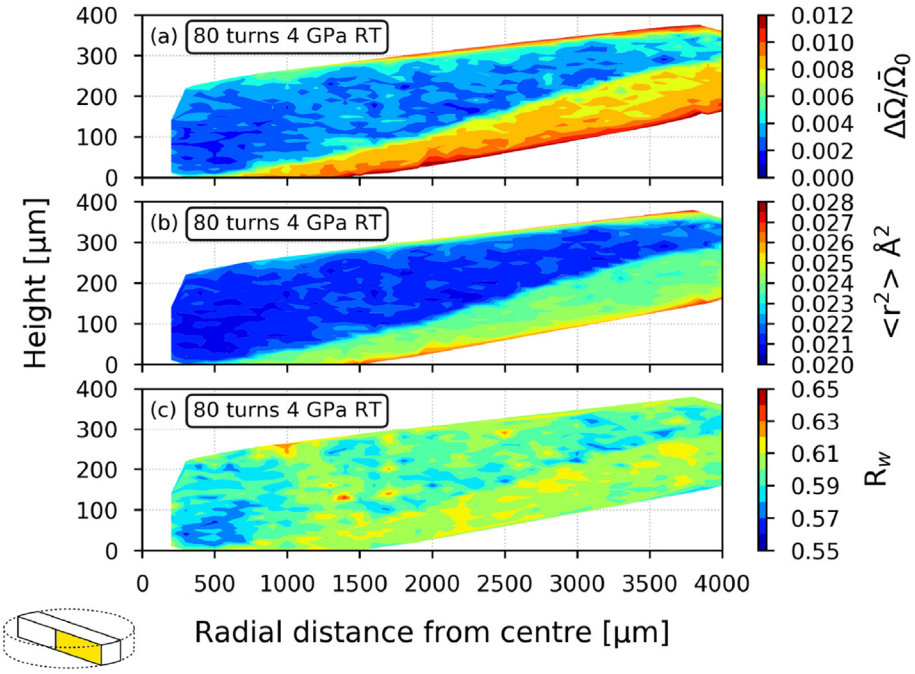

Fig. 7. Excess mean atomic volume $\Delta\overline{\Omega}$, mean square atomic displacement $<r^2>$ and plastic response R_w: (a) Position resolved $\Delta\overline{\Omega}/\overline{\Omega}_0$ of the rejuvenated material with respect to the as-cast state calculated from the local Young's modulus using the experimental relation shown in Fig. 6(c). (b) The mean square atomic displacement calculated from the flexibility volume shows an increase in the severely strained regions. (c) The change of $R_w = W_p/W_{tot}$ to higher values indicates an improved plastic behaviour in the rejuvenated regions. The as-cast sample shows an average value of $R_w = 0.599 \pm 0.008$.

BMGs can be drastically changed by rejuvenation. Detailed analysis on these changes promoting a more homogeneous like deformation in the severely strain softened regions of our HPT processed specimens will be presented elsewhere. Here, the plasticity criterion $R_w = W_{plastic}/W_{total}$ [19] is used to characterize the plastic response during nanoindentation, where $W_{plastic}$ and W_{total} are the work done by plastic and total deformation, respectively. Fig. 7(c) shows the position-dependent R_w values of the specimen processed by 80 turns, 4 GPa at RT. The as-cast specimen (not shown) has a value of $R_w = 0.599 \pm 0.008$. An increase of R_w in the rejuvenated regions is consistent with literature [19] and leads to the conclusion that plasticity in these regions is indeed enhanced. The reduction of shear steps surrounding the nanoindents as observed by AFM (cf. Fig. A4) strongly supports this interpretation and is in agreement with recent findings of HPT deformed specimens [19]. Consequently, we conclude that plastic flow in rejuvenated BMGs is more homogeneous, which is beneficial for the ductility.

4.4. Correlation between plastic and elastic properties

Metallic glasses show an empirical linear relationship between elastic and plastic properties for different compositions [50]. The hardness and Young's modulus scale by a relationship of the form $H = E/20$. We checked this relationship for differently modified structures using HPT by combining the nanoindentation data from the undeformed, deformed and severely deformed specimen states. In contrast to the previous studies where BMGs with different compositions were tested, in our case the changes in mechanical properties are induced by structural rejuvenation via plastic deformation. The experimental data cover the range from an undeformed (as-cast) state with low FV content up to a highly deformed state with saturated FV content. The relation from literature holds well for all samples when a small offset is added as can be seen by the linear fit to the data (black line) shown in Fig. 8. The best fit without offset (orange line) leads to a relation $H = 0.057E$. This demonstrates that by controlling the amount of plastic deformation during HPT, it is possible to tune the mechanical properties of BMGs within this reachable range.

5. Conclusions

In summary, we combined various experimental methods to systematically characterize structure and mechanical properties of a $Cu_{45}Zr_{45}Al_5Ag_5$ BMG processed by HPT under several deformation conditions (temperature, pressure, shear strain). It is shown that HPT of the BMG induces a rejuvenated amorphous structure characterized by an increased average free volume compared to the as-cast material. The structural change on the atomic level, that is stable over a long time at RT, is verified by both synchrotron X-ray diffraction and the energy release during heating. Based on the shift of the first synchrotron X-ray diffraction peak the local mean atomic volume is estimated. It varies considerably across the HPT disc and is increased up to about 0.75% for highly deformed regions with a saturated rejuvenated structure. The broadening of the first diffraction peak by strain-driven rejuvenation indicates an increased heterogeneity of the amorphous structure containing higher free volume contents. The calculated values for the flexibility volume as well as the mean square atomic displacement further show an increased atomic flexibility introduced by rejuvenation.

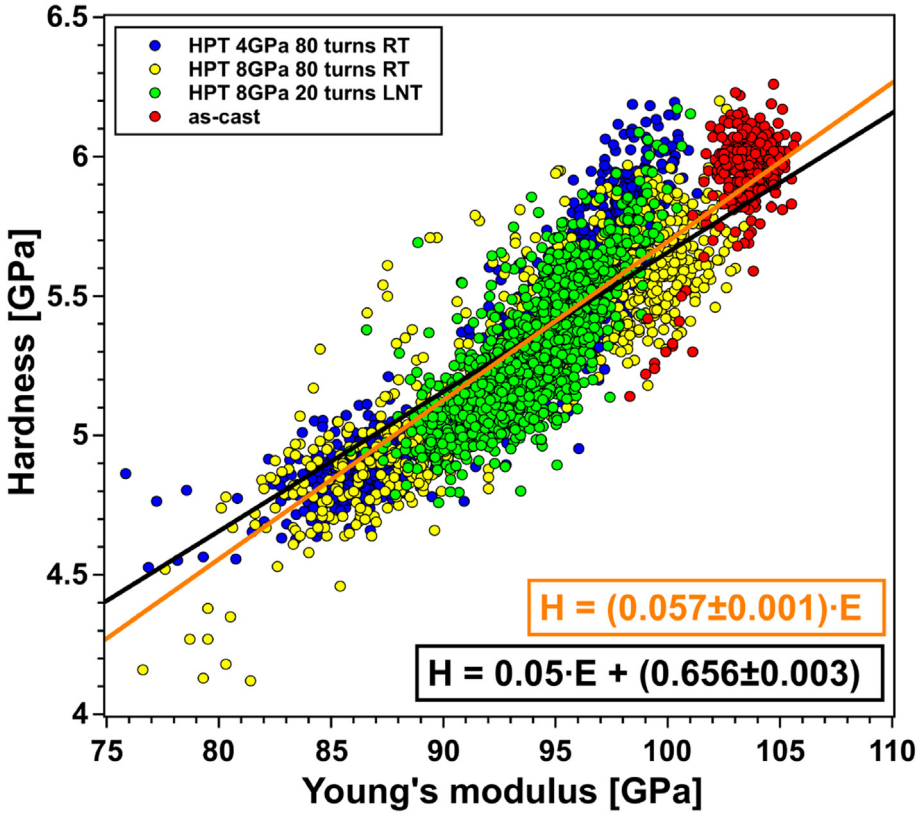

Fig. 8. Hardness as function of the Young's modulus: The hardness shows a linear relationship with the Young's modulus. The black line shows the fit of the linear relation $H = E/20 + d$ [50] to the data points. In addition, the best fit ($H = c \cdot E$) and its relation is indicated in orange. (For interpretation of the references to colour in this figure legend, the reader is referred to the Web version of this article.)

2-D mapping of both synchrotron X-ray data and local mechanical quantities measured by nanoindentation reveals a clear correlation of the rejuvenated amorphous structure attributed to free volume with both the elastic and plastic properties. Depending on the local free volume of the atomic structure, the Young's modulus and nanoindentation hardness decreases by as much as 20%. The measured relationship of the mean atomic volume with the Young's modulus was used to evaluate the excess mean atomic volume on the micron scale on the basis of nanoindentation measurements. Consequently, it is expected that elastic fluctuations triggered by the presence of excess mean atomic volume are distributed more heterogeneously on atomic scale in rejuvenated structures compared to as-cast structures.

Macroscopically, due to local strain softening the rejuvenated regions can be heterogeneously distributed and are not necessarily correlated to the nominal shear strain given by the HPT geometry. The spatially resolved maps recorded on cross-section of the HPT deformed specimens reveal a highly rejuvenated zone next to a less rejuvenated one. The volume fraction of the strain-softened zone increases slowly with increasing nominal accumulated shear strain. Therefore, uttermost care has to be taken with any integral measurements of samples deformed by HPT, e.g. simply measuring radial dependences might lead to wrong conclusions.

Strain softening of the rejuvenated structure is accompanied by an increase of the ratio R_w defining the plastic response during nanoindentation. In combination with AFM profiles of the indents it can be concluded that HPT significantly reduces the extent of strain localization and that structural rejuvenation promotes a more homogeneous-like plastic deformation. Therefore, controlling structural rejuvenation by HPT processing facilitates tailoring elastic and plastic properties within a given range.

Acknowledgements

We kindly acknowledge financial support by the Austrian Science Fund: I1309. This work was also supported by the Leibniz Program (Grant EC 111/261), as well as the German Federal Ministry of Education and Research BMBF (Project no. 05K2012). S.P. acknowledges support from DFG (grant no. PA2275/2-1). J.E. acknowledges the funding by the ERC Advanced Grant INTELHYB (grant ERC-2013-ADG-340025). We thank the European Synchrotron Radiation Facility for provision of the synchrotron radiation facilities and we would like to thank A. Poulain for assistance in using beamline ID31 during the beam time HC-2318.

Appendix A. Supplementary data

Supplementary data related to this article can be found at https://doi.org/10.1016/j.actamat.2018.08.032.

References

[1] A.L. Greer, Metallic glasses…on the threshold, Mater. Today 12 (1–2) (2009) 14–22, https://doi.org/10.1016/S1369-7021(09)70037-9.
[2] M. Ashby, A. Greer, Metallic glasses as structural materials, Scripta Mater. 54 (3) (2006) 321–326, https://doi.org/10.1016/j.scriptamat.2005.09.051.
[3] A. Greer, Y. Cheng, E. Ma, Shear bands in metallic glasses, Mater. Sci. Eng. R Rep. 74 (4) (2013) 71–132, https://doi.org/10.1016/j.mser.2013.04.001.
[4] V. Schmidt, H. Rösner, M. Peterlechner, G. Wilde, P.M. Voyles, Quantitative measurement of density in a shear band of metallic glass monitored along its propagation direction, Phys. Rev. Lett. 115 (3) (2015), https://doi.org/10.1103/PhysRevLett.115.035501, 035501.
[5] R. Maaß, K. Samwer, W. Arnold, C.A. Volkert, A single shear band in a metallic glass: local core and wide soft zone, Appl. Phys. Lett. 105 (17) (2014), https://doi.org/10.1063/1.4900791, 171902.
[6] C. Liu, V. Roddatis, P. Kenesei, R. Maaß, Shear-band thickness and shear-band cavities in a Zr-based metallic glass, Acta Mater. 140 (2017) 206–216, https://doi.org/10.1016/j.actamat.2017.08.032.
[7] H. Rösner, M. Peterlechner, C. Kübel, V. Schmidt, G. Wilde, Density changes in shear bands of a metallic glass determined by correlative analytical transmission electron microscopy, Ultramicroscopy 142 (2014) 1–9, https://doi.org/10.1016/j.ultramic.2014.03.006.
[8] R. Maaß, P. Birckigt, C. Borchers, K. Samwer, C. Volkert, Long range stress fields and cavitation along a shear band in a metallic glass: the local origin of fracture, Acta Mater. 98 (2015) 94–102, https://doi.org/10.1016/j.actamat.2015.06.062.
[9] C. Schuh, T. Hufnagel, U. Ramamurty, Mechanical behavior of amorphous alloys, Acta Mater. 55 (12) (2007) 4067–4109, https://doi.org/10.1016/j.actamat.2007.01.052.
[10] T.C. Hufnagel, C.A. Schuh, M.L. Falk, Deformation of metallic glasses: recent developments in theory, simulations, and experiments, Acta Mater. 109 (2016) 375–393, https://doi.org/10.1016/j.actamat.2016.01.049.
[11] E. Ma, J. Ding, Tailoring structural inhomogeneities in metallic glasses to enable tensile ductility at room temperature, Mater. Today 19 (10) (2016) 568–579, https://doi.org/10.1016/j.mattod.2016.04.001.
[12] J.S. Langer, Shear-transformation-zone theory of deformation in metallic glasses, Scripta Mater. 54 (3) (2006) 375–379, https://doi.org/10.1016/j.scriptamat.2005.10.005.
[13] J. Pan, Q. Chen, L. Liu, Y. Li, Softening and dilatation in a single shear band, Acta Mater. 59 (13) (2011) 5146–5158, https://doi.org/10.1016/j.actamat.2011.04.047.
[14] J.J. Lewandowski, a. L. Greer, Temperature rise at shear bands in metallic glasses, Nat. Mater. 5 (1) (2006) 15–18, https://doi.org/10.1038/nmat1536.
[15] S. Scudino, B. Jerliu, S. Pauly, K. Surreddi, U. Kühn, J. Eckert, Ductile bulk metallic glasses produced through designed heterogeneities, Scripta Mater. 65 (9) (2011) 815–818, https://doi.org/10.1016/j.scriptamat.2011.07.039.
[16] S.V. Ketov, Y.H. Sun, S. Nachum, Z. Lu, A. Checchi, A.R. Beraldin, H.Y. Bai, W.H. Wang, D.V. Louzguine-Luzgin, M.A. Carpenter, A.L. Greer, Rejuvenation of metallic glasses by non-affine thermal strain, Nature 524 (7564) (2015) 200–203, https://doi.org/10.1038/nature14674.
[17] F. Meng, K. Tsuchiya, Seiichiro, Y. Yokoyama, Reversible transition of deformation mode by structural rejuvenation and relaxation in bulk metallic glass, Appl. Phys. Lett. 101 (12) (2012), https://doi.org/10.1063/1.4753998, 121914.
[18] S.-H. Joo, D.-H. Pi, A.D.H. Setyawan, H. Kato, M. Janecek, Y.C. Kim, S. Lee, H.S. Kim, Work-hardening induced tensile ductility of bulk metallic glasses via high-pressure torsion, Sci. Rep. 5 (1) (2015) 9660, https://doi.org/10.1038/srep09660.
[19] J. Qiang, K. Tsuchiya, Composition dependence of mechanically-induced structural rejuvenation in Zr-Cu-Al-Ni metallic glasses, J. Alloy. Comp. 712 (2017) 250–255, https://doi.org/10.1016/j.jallcom.2017.04.096.
[20] Z. Kovács, E. Schafler, P. Szommer, Á. Révész, Localization of plastic deformation along shear bands in Vitreloy bulk metallic glass during high pressure torsion, J. Alloy. Comp. 593 (2014) 207–212, https://doi.org/10.1016/j.jallcom.2014.01.079.
[21] N. Adachi, Y. Todaka, Y. Yokoyama, M. Umemoto, Cause of hardening and softening in the bulk glassy alloy Zr 50 Cu 40 Al 10 after high-pressure torsion, Mater. Sci. Eng., A 627 (2015) 171–181, https://doi.org/10.1016/j.msea.2014.12.101.
[22] W. Dmowski, Y. Yokoyama, A. Chuang, Y. Ren, M. Umemoto, K. Tsuchiya, A. Inoue, T. Egami, Structural rejuvenation in a bulk metallic glass induced by severe plastic deformation, Acta Mater. 58 (2) (2010) 429–438, https://doi.org/10.1016/j.actamat.2009.09.021.
[23] T. Burgess, M. Ferry, Nanoindentation of metallic glasses, Mater. Today 12 (1–2) (2009) 24–32, https://doi.org/10.1016/S1369-7021(09)70039-2.
[24] C. Liu, R. Maaß, Elastic fluctuations and structural heterogeneities in metallic glasses, Adv. Funct. Mater. 1800388 (2018) 1–23, https://doi.org/10.1002/adfm.201800388.
[25] L. Wang, H. Bei, Y.F. Gao, Z.P. Lu, T.G. Nieh, Effect of residual stresses on the hardness of bulk metallic glasses, Acta Mater. 59 (7) (2011) 2858–2864, https://doi.org/10.1016/j.actamat.2011.01.025.
[26] F. Haag, D. Beitelschmidt, J. Eckert, K. Durst, Influences of residual stresses on the serrated flow in bulk metallic glass under elastostatic four-point bending - a nanoindentation and atomic force microscopy study, Acta Mater. 70 (2014) 188–197, https://doi.org/10.1016/j.actamat.2014.01.053.
[27] C. Gammer, B. Escher, C. Ebner, A.M. Minor, H.P. Karnthaler, J. Eckert, S. Pauly, C. Rentenberger, Influence of the Ag concentration on the medium-range order in a CuZrAlAg bulk metallic glass, Sci. Rep. 7 (2017), https://doi.org/10.1038/srep44903, 44903.
[28] W. Oliver, G. Pharr, Measurement of hardness and elastic modulus by instrumented indentation: advances in understanding and refinements to methodology, J. Mater. Res. 19 (01) (2004) 3–20, https://doi.org/10.1557/jmr.2004.19.1.3.
[29] N. Barekar, P. Gargarella, K. Song, S. Pauly, U. Kühn, J. Eckert, Effect of Al and Ag addition on phase formation, thermal stability, and mechanical properties of CuZr-based bulk metallic glasses, J. Mater. Res. 26 (14) (2011) 1702–1710, https://doi.org/10.1557/jmr.2011.61.
[30] D. Nečas, P. Klapetek, Gwyddion: an open-source software for SPM data analysis, Open Phys. 10 (1) (2012) 181–188, https://doi.org/10.2478/s11534-011-0096-2.
[31] B. Escher, U. Kühn, J. Eckert, C. Rentenberger, S. Pauly, Influence of Ag and Co additions on glass-forming ability, thermal and mechanical properties of Cu-Zr-Al bulk metallic glasses, Mater. Sci. Eng. 673 (2016) 90–98, https://doi.org/10.1016/j.msea.2016.06.081.
[32] C.J. Gilbert, J.W. Ager, V. Schroeder, R.O. Ritchie, J.P. Lloyd, J.R. Graham, Light

emission during fracture of a ZrTiNiCuBe bulk metallic glass, Appl. Phys. Lett. 74 (25) (1999) 3809–3811, https://doi.org/10.1063/1.124187.
[33] D. Ma, A.D. Stoica, X.-L. Wang, Power-law scaling and fractal nature of medium-range order in metallic glasses, Nat. Mater. 8 (1) (2009) 30–34, https://doi.org/10.1038/nmat2340.
[34] K.W. Park, C.M. Lee, M. Wakeda, Y. Shibutani, M.L. Falk, J.C. Lee, Elastostatically induced structural disordering in amorphous alloys, Acta Mater. 56 (19) (2008) 5440–5450, https://doi.org/10.1016/j.actamat.2008.07.033.
[35] P. Ross, S. Küchemann, P.M. Derlet, H.B. Yu, W. Arnold, P. Liaw, K. Samwer, R. Maaß, Linking macroscopic rejuvenation to nano-elastic fluctuations in a metallic glass, Acta Mater. 138 (2017) 111–118, https://doi.org/10.1016/j.actamat.2017.07.043.
[36] S. Küchemann, R. Maaß, Gamma relaxation in bulk metallic glasses, Scripta Mater. 137 (2017) 5–8, https://doi.org/10.1016/j.scriptamat.2017.04.034.
[37] R. Pippan, S. Scheriau, A. Taylor, M. Hafok, A. Hohenwarter, A. Bachmaier, Saturation of fragmentation during severe plastic deformation, Annu. Rev. Mater. Res. 40 (1) (2010) 319–343, https://doi.org/10.1146/annurev-matsci-070909-104445.
[38] D. Geist, C. Rentenberger, H. Karnthaler, Extreme structural inhomogeneities in high-pressure torsion samples along the axial direction, Acta Mater. 59 (11) (2011) 4578–4586, https://doi.org/10.1016/j.actamat.2011.04.003.
[39] Á. Révész, E. Schafler, Z. Kovács, Structural anisotropy in a Zr57Ti5-Cu20Al10Ni8 bulk metallic glass deformed by high pressure torsion at room temperature, Appl. Phys. Lett. 92 (1) (2008), https://doi.org/10.1063/1.2830992, 011910.
[40] Z. Kovács, E. Schafler, Á. Révész, Volume changes in Vitreloy bulk metallic glass during room temperature high-pressure torsion, J. Mater. Res. 23 (12) (2008) 3409–3414, https://doi.org/10.1557/JMR.2008.0416.
[41] R.B. Figueiredo, M.T.P. Aguilar, P.R. Cetlin, T.G. Langdon, Analysis of plastic flow during high-pressure torsion, J. Mater. Sci. 47 (22) (2012) 7807–7814, https://doi.org/10.1007/s10853-012-6506-z.
[42] J. Ding, M. Asta, R.O. Ritchie, On the question of fractal packing structure in metallic glasses, Proc. Natl. Acad. Sci. Unit. States Am. 114 (32) (2017) 8458–8463, https://doi.org/10.1073/pnas.1705723114.
[43] M. Jiang, G. Wilde, J. Gao, L. Dai, A universal power law for metallic glasses, Scripta Mater. 69 (10) (2013) 760–763, https://doi.org/10.1016/j.scriptamat.2013.08.022.
[44] J. Ding, Y.Q. Cheng, H. Sheng, M. Asta, R.O. Ritchie, E. Ma, Universal structural parameter to quantitatively predict metallic glass properties, Nat. Commun. 7 (2016) 1–10, https://doi.org/10.1038/ncomms13733.
[45] A. Slipenyuk, J. Eckert, Correlation between enthalpy change and free volume reduction during structural relaxation of Zr55Cu30Al10Ni5 metallic glass, Scripta Mater. 50 (1) (2004) 39–44, https://doi.org/10.1016/j.scriptamat.2003.09.038.
[46] Y. Zhang, H. Hahn, Quantification of the free volume in Zr45.0Cu39.3A-l7.0Ag8.7 bulk metallic glasses subjected to plastic deformation by calorimetric and dilatometric measurements, J. Alloy. Comp. 488 (1) (2009) 65–71, https://doi.org/10.1016/j.jallcom.2009.08.091.
[47] C. Schuh, T. Nieh, A survey of instrumented indentation studies on metallic glasses, J. Mater. Res. 19 (01) (2004) 46–57, https://doi.org/10.1557/jmr.2004.19.1.46.
[48] A.L. Greer, A. Castellero, S.V. Madge, I.T. Walker, J.R. Wilde, Nanoindentation studies of shear banding in fully amorphous and partially devitrified metallic alloys, Mater. Sci. Eng., A 375–377 (2004) 1182–1185, https://doi.org/10.1016/j.msea.2003.10.032.
[49] P. Denis, C.M. Meylan, C. Ebner, A.L. Greer, M. Zehetbauer, H.J. Fecht, Rejuvenation decreases shear band sliding velocity in Pt-based metallic glasses, Mater. Sci. Eng., A 684 (2017) 517–523, https://doi.org/10.1016/j.msea.2016.12.075.
[50] W.H. Wang, The elastic properties, elastic models and elastic perspectives of metallic glasses, Prog. Mater. Sci. 57 (3) (2012) 487–656, https://doi.org/10.1016/j.pmatsci.2011.07.001.